Check for updates

AGU PUBLICATIONS

Radio Science

RESEARCH ARTICLE
10.1002/2017RS006263

Key Points:
- A new technique exploiting oblique Digisonde-to-Digisonde skymap observations is implemented to directly identify TID in real time
- The ionosphere is represented by a moving undulated mirror, to relate HF signal parameters to TID characteristics, using the FAS technique
- The performance is demonstrated during a period of moderate auroral activity and assessed in respect to prevailing geophysical conditions

Correspondence to:
A. Belehaki,
belehaki@noa.gr

Citation:
Reinisch, B., Galkin, I., Belehaki, A., et al. (2018). Pilot ionosonde network for identification of traveling ionospheric disturbances. *Radio Science*, *53*, 365–378. https://doi.org/10.1002/2017RS006263

Received 1 FEB 2017
Accepted 17 FEB 2018
Accepted article online 24 FEB 2018
Published online 30 MAR 2018

©2018. The Authors.
This is an open access article under the terms of the Creative Commons Attribution-NonCommercial-NoDerivs License, which permits use and distribution in any medium, provided the original work is properly cited, the use is non-commercial and no modifications or adaptations are made.

Pilot Ionosonde Network for Identification of Traveling Ionospheric Disturbances

Bodo Reinisch[1,2], Ivan Galkin[2], Anna Belehaki[3], Vadym Paznukhov[4], Xueqin Huang[1], David Altadill[5], Dalia Buresova[6], Jens Mielich[7], Tobias Verhulst[8], Stanimir Stankov[8], Estefania Blanch[5], Daniel Kouba[6], Ryan Hamel[1], Alexander Kozlov[2], Ioanna Tsagouri[3], Angelos Mouzakis[3], Mauro Messerotti[9], Murray Parkinson[10], and Mamoru Ishii[11]

[1]Lowell Digisonde International, Lowell, MA, USA, [2]Space Science Laboratory, University of Massachusetts Lowell, Lowell, MA, USA, [3]National Observatory of Athens, IAASARS, Penteli, Greece, [4]Institute for Scientific Research, Boston College, Chestnut Hill, MA, USA, [5]Observatori de l'Ebre, CSIC, Universitat Ramon Llull, Roquetes, Spain, [6]Institute of Atmospheric Physics, Czech Academy of Sciences, Prague, Czech Republic, [7]Leibniz-Institute of Atmospheric Physics, Kühlungsborn, Germany, [8]Royal Meteorological Institute, Brussels, Belgium, [9]INAF, Trieste, Italy, [10]Space Weather Services, Australian Bureau of Meteorology, Melbourne, Victoria, Australia, [11]National Institute of Information and Communications Technology, Tokyo, Japan

Abstract Traveling ionospheric disturbances (TIDs) are the ionospheric signatures of atmospheric gravity waves. Their identification and tracking is important because the TIDs affect all services that rely on predictable ionospheric radio wave propagation. Although various techniques have been proposed to measure TID characteristics, their real-time implementation still has several difficulties. In this contribution, we present a new technique, based on the analysis of oblique Digisonde-to-Digisonde "skymap" observations, to directly identify TIDs and specify the TID wave parameters based on the measurement of angle of arrival, Doppler frequency, and time of flight of ionospherically reflected high-frequency radio pulses. The technique has been implemented for the first time for the Network for TID Exploration project with data streaming from the network of European Digisonde DPS4D observatories. The performance is demonstrated during a period of moderate auroral activity, assessing its consistency with independent measurements such as data from auroral magnetometers and electron density perturbations from Digisondes and Global Navigation Satellite System stations. Given that the different types of measurements used for this assessment were not made at exactly the same time and location, and that there was insufficient coverage in the area between the atmospheric gravity wave sources and the measurement locations, we can only consider our interpretation as plausible and indicative for the reliability of the extracted TID characteristics. In the framework of the new TechTIDE project (European Commission H2020), a retrospective analysis of the Network for TID Exploration results in comparison with those extracted from Global Navigation Satellite System total electron content-based methodologies is currently being attempted, and the results will be the objective of a follow-up paper.

1. Introduction

Traveling ionospheric disturbances (TIDs) play an important role in the momentum and energy exchange between various regions of the upper atmosphere and in the coupling between the neutral atmosphere and ionospheric plasma (e.g., Belehaki et al., 2016; Federenko et al., 2014; Hines, 1974; Hocke & Schlegel, 1996). TIDs impose disturbances in the ionospheric electron density distribution, and consequently perturbations in the total electron content (TEC), that may affect the normal operation of systems depending on ground-based high-frequency (HF) and transionospheric very high frequency-ultrahigh frequency radiowave propagation (e.g., Davies, 1990; McNamara, 1991).

TIDs usually cause TEC changes of up to 10 total electron content unit (TECU) depending on their wavelength. TIDs can also impose Doppler frequency shifts of the order of 0.5 Hz on HF signals. Usually, they are classified as either large-scale TIDs (LSTIDs) or medium-scale TIDs (MSTIDs). LSTIDs propagate with wavelengths of 1,000 to 3,000 km and velocities of 300–1,000 m/s. Their amplitudes are greater than 5–10 TECU, and they are associated with auroral and geomagnetic activity (e.g., Tsugawa et al., 2004). During geomagnetic storms, the rapid intensification of auroral electrojets leads to the heating of the upper atmosphere. The rapid expansion and further compression of the atmosphere generates atmospheric gravity waves (AGWs) that

19447973, 2018, 3, Downloaded from https://agupubs.onlinelibrary.wiley.com/doi/10.1002/2017RS006263 by Cochrane Germany, Wiley Online Library on [20/12/2022]. See the Terms and Conditions (https://onlinelibrary.wiley.com/terms-and-conditions) on Wiley Online Library for rules of use; OA articles are governed by the applicable Creative Commons License

propagate equatorward (Prölss & Ocko, 2000). Compression-refraction of the plasma densities by the divergence of the AGW motion produces LSTIDs. The density variations generate variations in the height of the electron isodensity surfaces. These height variations influence the paths of HF radio waves (e.g., MacDougall et al., 2009; Yakovets et al., 2013).

MSTIDs propagate with wavelengths of ~100–300 km and a velocity of ~100 m/s (Chilcote et al., 2015), and they are often associated with ionospheric coupling from below, in which case there is no clear correlation with the geomagnetic activity, making their identification more difficult. The majority of MSTIDs cause TEC changes of less than 1 TECU; however, super MSTIDs with amplitudes reaching 10 TECU have occasionally been observed (Hernandez-Pajares et al., 2006). Recently, Ding et al. (2013) reported observations of poleward propagation of LSTIDs. It was suggested that energy dissipation from MSTIDs of lower atmosphere origin (e.g., Crane, 2017; Liu, 2016) can excite secondary LSTIDs that could propagate in the poleward direction, thus excluding the auroral regions as the primary source of such disturbances.

LSTIDs affect the performance of Satellite-Based Augmentation Systems, such as the European Geostationary Navigation Overlay Service (Chaggara et al., 2015; Pintor & Roldan, 2015), as they can induce variations in TEC of several TECUs. MSTIDs, known to occur at any time with varying amplitudes, similar to cloud occurrences in the troposphere, can tilt the reflecting isodensity contours by up to 3° to 5°. These time-varying tilts cause variances in the measured bearings of about 1° for emitter distances of 1,000 km to about 100° for 100 km, the "short-range catastrophe" (Ross, 1947). Hernandez-Pajares et al. (2006) have shown that MSTIDs can affect the performance of high accuracy navigation systems, like Network Real-Time Kinematics, that are based on interpolating the ionospheric delays.

Regarding the over-the-horizon radar performance, TIDs remain a troubling cause of error for the coordinate registration. They are the principal remaining ionospheric feature that limits the performance of target detection algorithms for over-the-horizon radars because the associated range/azimuth deflections spread the target return in the algorithm results. In a series of measurements, when the U.S. Navy Relocatable Over-the-Horizon Radar, AN/TPS-71 dwelled on a fixed beacon for long periods of time, the beacon appeared to move several tens of kilometers within a few minutes. These apparent motions are likely due to TIDs (e.g., Nickisch et al., 2006).

A widely used TID identification technique is based on the exploitation of maps of vertical TEC values derived from slant TEC measurements with the ground-based Global Navigation Satellite System (GNSS) receiver network (e.g., Borries et al., 2009, 2016; Ding et al., 2007). The performance of this approach has been successfully demonstrated for postevent analysis. However, there are some issues to be considered such as the limitations imposed from the algorithms inverting the slant to the vertical TEC and the applied "data smoothing" that might inadvertently mask the TIDs. Considering also that the largest density variations during TIDs occur at or below the F_2 layer peak in the ionosphere, while approximately two thirds of TEC is located in the topside ionosphere and the plasmasphere, direct measurements of the bottomside electron densities will likely provide a more accurate assessment of the bottomside TIDs.

Ionosondes have been used for a long time to monitor the TID activity in the bottomside ionosphere (e.g., Morgan et al., 1978; Tedd & Morgan, 1985). In this paper, we present a direct method for the detection of bottomside TIDs based on the use of bistatic HF propagation links between DPS4D Digisondes (Reinisch et al., 2009) that allow the real-time identification and specification of TIDs through the analysis of oblique Digisonde-to-Digisonde (D2D) "skymap" observations. Establishment of such a measurement network is the objective of the Network for TID Exploration (Net-TIDE) project (Belehaki et al., 2015). The Net-TIDE synchronized ionosonde network is described in a companion paper (Verhulst et al., 2017). Section 2 describes the TID model used for the analysis, and the Doppler-Frequency-Angular-Sounding (FAS) TID analysis technique (Paznukhov et al., 2012). From the D2D skymap observations of the angles of arrival (AoA), time of flight (ToF), and Doppler frequency of ionospherically reflected HF radio signals, the characteristics of the TID waves, especially the amplitude A_N and the propagation direction Θ, are computed in order to nowcast the TID activity in the region. A case study of a TID event over Europe is discussed in section 3 illustrating the technique. The assessment of the extracted TID characteristics in respect to prevailing geophysical conditions is discussed in section 4, and the main findings are summarized in section 5.

1944799x, 2018, 3, Downloaded from https://agupubs.onlinelibrary.wiley.com/doi/10.1002/2017RS006263 by Cochrane Germany, Wiley Online Library on [20/12/2022]. See the Terms and Conditions (https://onlinelibrary.wiley.com/terms-and-conditions) on Wiley Online Library for rules of use; OA articles are governed by the applicable Creative Commons License

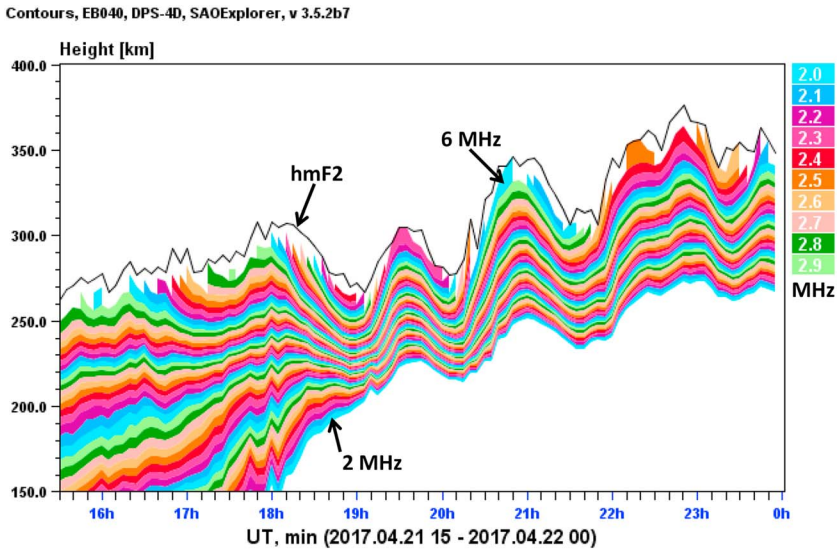

Figure 1. Traveling ionospheric disturbance signature in the electron isodensity contours derived from Digisonde vertical ionogram meaurements at the Ebro Observatory (Roquetes, Spain).

2. TID Model and the FAS Technique

Vertical HF soundings with ionosondes routinely measure the vertical electron density profiles (e.g., Reinisch & Huang, 1983) and their variations during the passage of a TID over a station. The time series of electron density profiles as a function of time reveals the arrival of the disturbance and may show quasiperiodic height variations of the isodensity contours during the passage of a TID as illustrated in Figure 1. The Ebro/Roquetes Digisonde measurements from 21 April 2017 show a distinct quasiperiodic wave structure starting at ~19 UT with periods of about 70 min and longer and amplitudes A_C of ~20–40 km. The isodensity contours in Figure 1 are identified by their corresponding electron plasma frequency f_N indicated by different colors; the color sequence repeats every 10 lines, that is, at 3.0 MHz, 4.0 MHz, etc. The corresponding electron densities are $N_e[\mathrm{m}^{-3}] = 1.26\times10^{10} f_N^2[\mathrm{MHz}^2]$. While the amplitudes and periods of TID waves at the ionosonde locations can be estimated from such isodensity contour plots, the direction of the wave propagation cannot. The D2D skymap measurements of TIDs described in section 2.2 provide this additional information.

2.1. TID Model

We assume that the disturbed ionospheric electron density distribution can be considered a superposition of horizontally propagating sinusoidal plane waves and that at height z_0 each wave can be represented as a function of x, y, and time t by (Huang et al., 2016)

$$N(z_0,t;x,y) = N_{\mathrm{bg}}(z_0,t;x,y)\left[1+\sum_i A_{Ni}\ \cos\{\Omega_i t - K_i[x\cos\Theta_i + y\sin\Theta_i] + \Phi_{0i}\}\right]. \quad (1)$$

Here N_{bg} is the undisturbed background density distribution; Φ_0 is the initial phase; $\Omega/2\pi$ is the frequency, commonly presented as its reciprocal, the wave period T_Ω; and $K = 2\pi/\Lambda$ is the wave number, where Λ is the wavelength. The component "i" with the maximum amplitude A_{Ni} is currently used for the FAS TID analysis described in section 2.2. Huang et al. (2016), using the Huang and Reinisch (2006) ray tracing code, have verified that the time variations of the measured HF signal parameters are equivalent to those of a free-space signal reflected at a sinusoidally undulated mirror at height z_0 moving with velocity V_p. This mirror is represented by the dashed line in Figure 2. The amplitude A_C of the isodensity contour wave relates to the amplitude A_N of the corresponding horizontal density modulation at height z_0 according to $A_N = \frac{1}{N(z_0)}\frac{\partial N}{\partial z}A_C$. The altitude z_0 of the reflecting mirror can be estimated using the average, ε_0, of the measured elevation angles $\varepsilon(t)$ of the arriving signals and the ground distance G_{TR} between transmitter and receiver, $z_0 = \frac{1}{2}G_{\mathrm{TR}}\tan(\varepsilon_0)$.

1944799x, 2018, 3, Downloaded from https://agupubs.onlinelibrary.wiley.com/doi/10.1002/2017RS006263 by Cochrane Germany, Wiley Online Library on [20/12/2022]. See the Terms and Conditions (https://onlinelibrary.wiley.com/terms-and-conditions) on Wiley Online Library for rules of use; OA articles are governed by the applicable Creative Commons License

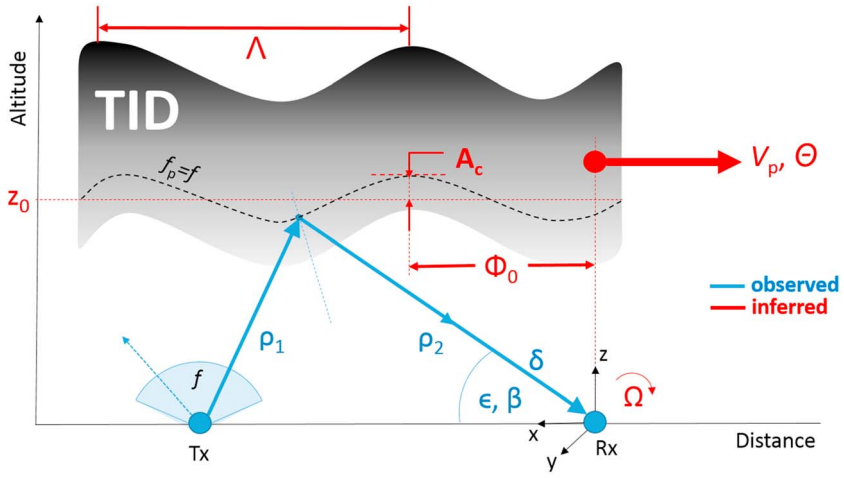

Figure 2. Traveling ionospheric disturbance (TID) model as a perfectly reflecting corrugated mirror (dashed line) moving across the area (red arrow) and causing variations of the oblique-incidence signal (blue line) characteristics {$\rho(t)$, $\delta(t)$, $\varepsilon(t)$, and $\beta(t)$}.

For the mirror model the signal path length ρ for each ray is simply the sum of the two straight segments ρ_1 and ρ_2. As the TID moves across the reflection area, the signals arriving at the receiver exhibit quasi-sinusoidal variations of its radio frequency (RF) signal characteristics: elevation $\varepsilon(t)$ and azimuth $\beta(t)$, Doppler frequency $\delta(t)$, and time of flight $\tau(t)$ (or the equivalent group path $\rho(t) = c \cdot \tau(t)$, where c is the free-space speed of light). The transmitter *Tx* emits radio waves at operating frequency f into a wide beam, and several signals (rays) can reach the receiver *Rx* using different modes of propagation.

2.2. Inferring TID Parameters From Observed HF Signals

Representing the ionosphere by a moving undulated mirror facilitates relating the measured signal parameters to the characteristics of the propagating waves using the Doppler-FAS technique (Beley et al., 1995; Galushko et al., 2003; Paznukhov et al., 2012). While the time series of all signal characteristics {$\rho(t)$, $\delta(t)$, $\varepsilon(t)$, and $\beta(t)$} vary with the wave period T_Ω, the Doppler frequency variation $\delta(t)$ proved to be the most reliable indicator for the detection of quasi-sinusoidal variations. The FAS analysis therefore first calculates the spectrum $S_\delta(\Omega)$ running a fast Fourier transform on the input $\delta(t)$ time series, repeating the calculations for a set of analysis time windows varying from ~40 min to 160 min. Beley et al. (1995) had derived the relations between the wave parameters and the RF signal variations:

$$A_N = \left| i\widetilde{S}_\delta \frac{\lambda}{2\Omega z_0 \sin \varepsilon_0} \right| \tag{2}$$

$$K = \frac{2\pi}{\Lambda} = \left| \frac{\cos \varepsilon_0}{z_0 \lambda \widetilde{S}_\delta} \widetilde{Q} \right|; \quad V_p = \frac{\Omega}{K} \tag{3}$$

$$\Theta = \mathrm{Re}\left(\arctan\left(\frac{-i\lambda\widetilde{S}_\delta + 2z_0\Omega\widetilde{S}_\varepsilon \tan \varepsilon_0}{\widetilde{Q}}, \frac{-2z_0\Omega\widetilde{S}_\beta}{\widetilde{Q}} \right) \right) \tag{4}$$

$$\widetilde{Q} = \sqrt{-\widetilde{S}_\delta^2\lambda^2 \sin^2\varepsilon_0 - i4z_0\lambda\Omega\widetilde{S}_\delta\widetilde{S}_\varepsilon \sin \varepsilon_0 \tan \varepsilon_0 + 4z_0^2\Omega^2\left(\widetilde{S}_\varepsilon^2 \tan^2 \varepsilon_0 + \widetilde{S}_\beta^2\right)}. \tag{5}$$

Here $\lambda = c/f$ is the free-space wavelength of the signal carrier at transmission frequency f. The Beley relations assume that a single RF signal arrives at the receiver. Because of the large radiation beam width of the Digisonde's transmit antenna (see Verhulst et al., 2017) multiple rays usually propagate to the receiver using different ionospheric propagation modes, for example, 1F2L (i.e., 1-hop F_2 layer reflection and low-angle ray), 1F2H (high-angle ray), and 1F1L (1-hop F1 and low-angle ray). The receiving system must be able to separate and identify the different rays and find continuous time series of the observables {$\rho_m(t)$, $\delta_m(t)$, $\varepsilon_m(t)$, and $\beta_m(t)$} so that the respective Fourier transforms for the selected propagation mode m can be calculated. Section 3 discusses the signal processing techniques that have been developed to separate these different signals.

1944799x, 2018, 3, Downloaded from https://agupubs.onlinelibrary.wiley.com/doi/10.1002/2017RS006263 by Cochrane Germany, Wiley Online Library on [20/12/2022]. See the Terms and Conditions (https://onlinelibrary.wiley.com/terms-and-conditions) on Wiley Online Library for rules of use; OA articles are governed by the applicable Creative Commons License

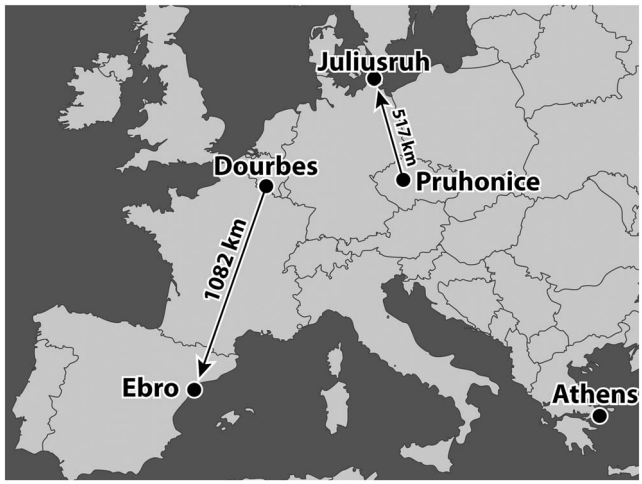

Figure 3. DPS4 observatories and the Digisonde-to-Digisonde skymap links DB → EB and PQ → JR that operated during the case study. The Athens DPS4D, the fifth station of the network, contributed to this event with electron density profile data (see Table 1). DB = Dourbes; EB = Ebro; PQ = Pruhonice; JR = Juliusruh.

The method of making oblique D2D skymap measurements for the calculation of the TID characteristics has been implemented in several DPS4D ionospheric stations operating in Europe. This was possible because of the advanced capabilities offered by the DPS4D ionosonde (Reinisch et al., 2009). In summary, DPS4Ds have digital transmitters and receivers in which no analog circuitry is used for conversion from the RF to the baseband. In contrast to the older Digisondes, the new hardware design has enabled the implementation of new software solutions that offer significantly enhanced measurement flexibility, enhanced signal selectivity, and new types of data, for example, the complete set of time domain samples of all four receive antenna signals suitable for independent scientific analysis (DPS4D Technical Manual, 2014). With a new method of mitigating in-band RF interference, the ionogram running time can be made as short as a couple of seconds even though the transmitted RF power is less than 15 W_{ave}. These capabilities make successful observations possible in an electromagnetically polluted area like Europe. The precision ranging technique (Reinisch et al., 2008) with an accuracy of better than 1 km routinely measures the virtual height $h'(f) = c \cdot \tau(f)/2$. The DPS4D runs the new ARTIST-5 ionogram autoscaling software (Galkin et al., 2008), which provides in real time the required data for the assimilation in ionospheric models (Galkin et al., 2012), especially the International Reference Ionosphere model (Bilitza et al., 2014).

3. Case Study

In a companion paper Verhulst et al. (2017) described the implementation of automated programs for the D2D skymap measurements. Figure 3 and Table 1 show the locations of the participating European Digisonde observatories. Since each observatory conducts its independent routine measurement program the D2D skymap measurements must be squeezed into available time slots. During the time of the case study (21 April 2017), only two D2D links were continuously operating as indicated in Figure 3.

3.1. D2D Skymap Measurements

In April 2017, two D2D links routinely made 10 s D2D skymap measurements every 5 min. Figures 4 and 5 show results of measurements at 17:47 UT on 21 April 2017 for the PQ → JR link, and at 17:48 UT for the DB → EB link. The Doppler waterfall display shows the spectral signal amplitudes measured at consecutive group path lengths spaced by 5 km (corresponding to 16.66 μs increments in the time of flight of the RF pulses). Each of the RF signatures that exceeds the detection threshold, indicated by a dotted circle in the waterfall display, is processed to determine its angles of arrival. These angles specify the location of the signature on the accompanying D2D skymap (Figures 4 and 5, right). The skymap displays use a Cartesian representation of the arrival angles in a north-south and east-west angle coordinate system where α_{NS}[degrees] = (90 − ε) cos (β + 90), and α_{EW}[degrees] = (90 − ϵ) sin (β + 90).

There usually are tens or hundreds of signatures that are placed as "sources" on a given skymap, each with its own group path and Doppler frequency. An intelligent *signal clustering* system assigns each source on the skymap to a specific "signal cluster." The clustering operation performs as a bottom-up hierarchical grouping that starts with each signature being an individual cluster and then iteratively groups "compatible" sources into one cluster (e.g., Murtagh & Contreras, 2012). Compatibility of signatures is determined by testing which signals arrive with similar group path ρ, similar Doppler frequency δ, and comparable arrival angles. The hierarchical grouping stops automatically, without human analyst supervision, when no more compatible clusters can be found to combine them. Most frequently, such stop condition occurs when all available clusters are separated by at least 1 bin of the group path, which means that signal propagation modes are distinctly different in their time of flight. When different signal propagation modes overlap in arrival time, their separation is made possible by differences in the Doppler frequency and/or the AoAs. When all clusters are separated by gaps in ToF, AoA, and Doppler frequency, the clustering process stops. For the skymap example shown in Figure 4, right, four distinct clusters were

1944799x, 2018, 3, Downloaded from https://agupubs.onlinelibrary.wiley.com/doi/10.1002/2017RS006263 by Cochrane Germany, Wiley Online Library on [20/12/2022]. See the Terms and Conditions (https://onlinelibrary.wiley.com/terms-and-conditions) on Wiley Online Library for rules of use; OA articles are governed by the applicable Creative Commons License

Table 1
DPS4D Observatories Forming the Net-TIDE Network

Observatory	Latitude	Longitude	Isodensity contours (EDP data)	D2D skymaps
Juliusruh, JR	54.6	13.4	X	PQ → JR
Dourbes, DB	50.1	4.6	X	DB → EB
Pruhonice, PQ	50.0	14.6	X	PQ → JR
Ebro, EB	40.8	0.50	X	DB → EB
Athens, AT	38.0	23.5	X	

Note. EDP = electron density profile; D2D = Digisonde-to-Digisonde; Net-TIDE, Network for TID Exploration.

determined (shown with different symbols) that belong to different propagation modes. The *average* arrival angle and the average Doppler frequency for each cluster serve as the potential inputs to the FAS analysis.

The propagation modes for these identified signals are determined by comparison with results from simulated ray tracing through the assimilative International Reference Ionosphere model IRTAM (Galkin et al., 2012) as illustrated in Figure 6, right. For the example in Figure 4, the high- and low-angle 1-hop *E* layer reflections, 1EH and 1EL, and the 1F2H and 2F2H rays were identified. This identification process is currently performed manually; 1-hop *E* layer reflections are automatically excluded by disregarding signals with ToFs that are smaller than a calculated maximum ToF possible for an *E*-mode signal propagating from transmitter to receiver at the given time of day.

To calculate the Fourier transforms used in the FAS, equations (2)–(5) require a series of consecutive data samples for the signal (propagation mode) selected for analysis. Each signal is therefore tracked from skymap to skymap using an intelligent *signal tracker* algorithm, which identifies consistent time samples for each signal as illustrated in Figure 6. The signal tracker developed for this task is based on the Artificial Neural Network pre-Attentive Eye model of human vision that had previously been used successfully in the ARTIST-5 ionogram autoscaling software (Galkin et al., 1996, 2008). Figure 6, left shows only two consistent tracks of consistent group path values, one at ~660 km, the other at ~560 km; "noise" signals are shown as isolated circles. In this simple example, it is easy to identify these tracks as 1EL and 1F2L modes by comparison with the synthesized ionogram shown in Figure 6, right.

Multiple mode propagation conditions can lead to a multitude of signal tracks as illustrated in Figure 7 showing results for the 1,083 m long DB → EB 9.10 MHz link on 21 April 2017. Before ~16 UT the measured Doppler frequencies (top left panel) show only small variations. The −1.85 Hz Doppler frequency bias is caused by a small difference in the frequency standards at the transmitting and receiving ionosondes and is automatically removed in the FAS analysis. The Doppler frequency variations become large after ~16 UT, and the jitter on the angle tracks, especially the zenith angle, reduces. For illustration, a 120 min track section of the 1F2H mode signals is highlighted in blue in all panels. For the FAS TID analysis we only used the 1F2L tracks.

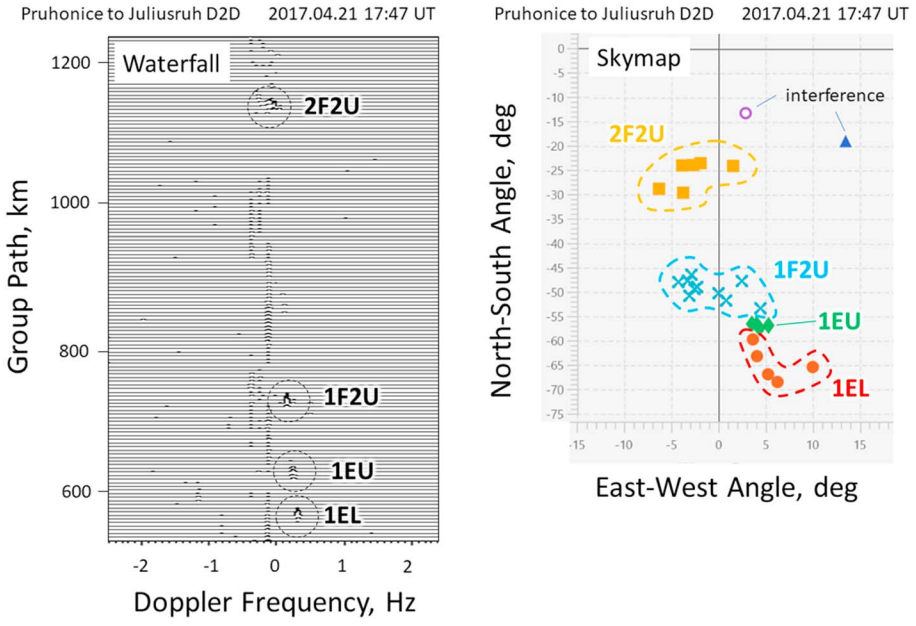

Figure 4. Digisonde-to-Digisonde (D2D) measurements for northern Pruhonice to Juliusruh link, f = 5.05 MHz; Doppler waterfall and skymap.

1944799x, 2018, 3, Downloaded from https://agupubs.onlinelibrary.wiley.com/doi/10.1002/2017RS006263 by Cochrane Germany, Wiley Online Library on [20/12/2022]. See the Terms and Conditions (https://onlinelibrary.wiley.com/terms-and-conditions) on Wiley Online Library for rules of use; OA articles are governed by the applicable Creative Commons License

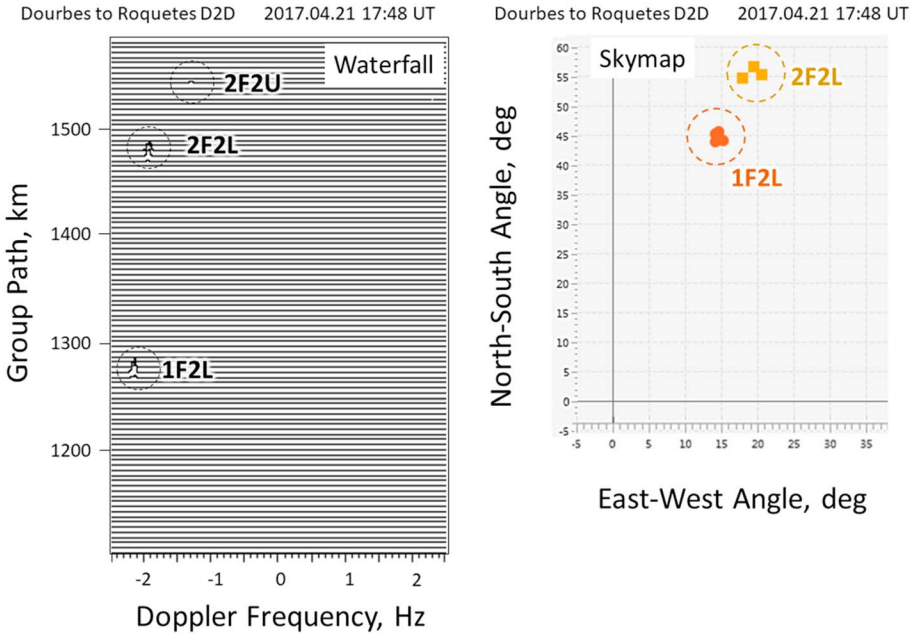

Figure 5. Same as Figure 4 but for southern Dourbes to Ebro link, $f = 9.10$ MHz.

3.2. First Results

Results of a case study for 21–22 April 2017 are shown in Figure 8, which displays the amplitudes and propagation directions for the dominant TID waves from 05 UT to 05 UT the next day. Since TID amplitudes are expected to be stronger in the *F* region than in the *E* region, we have included only 1F2L mode RF signals in the FAS analysis. We believe that the high-angle or slow ray 1F2H is not well represented by the mirror reflection model. Weak RF signals with signal-to-noise ratios (SNRs) smaller than 20 dB were not included in the FAS analysis. The time axis is dashed when no data were available or the SNR was smaller than 20 dB.

Before 18 UT, only TIDs with small amplitudes (<20%) were detected on both links. The propagation direction is predominantly southward with azimuth angles varying between 120° and 240°. Large-amplitude TIDs were detected during the next 8 h on both links. From 18 UT to 19 UT the propagation angle is ~120° on both links and then jumps to ~60° at 19 UT. After 20 UT, the north link shows predominantly south and southwestward propagation, the south link northeastward and southeastward propagation.

All measured D2D ionogram and skymap data were ingested in real time via Internet in databases at the Lowell Global Ionosphere Radio Observatory (GIRO) Data Center, http://giro.uml.edu/ (Reinisch & Galkin, 2011). The D2D skymap data and the FAS analysis results are archived in a new TID database, TIDBase, https://lgdc.uml.edu/tidx/. During this project all signal processing of the measured skymap data and the FAS analysis has been performed at Lowell GIRO Data Center. To enable retrospective analysis of past data, TIDBase also stores

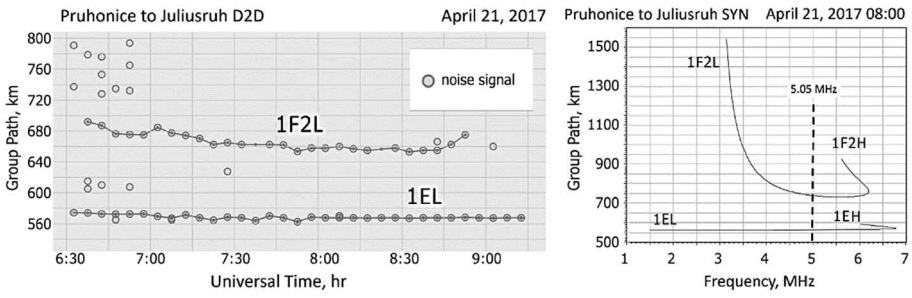

Figure 6. (left) Automatically tracked signal group path tracks for the 512 km PQ → JR (5.05 MHz) link. (right) The synthesized oblique ionogram for 08:00 UT. JR = Juliusruh; PQ = Pruhonice; D2D = Digisonde-to-Digisonde.

19447973x, 2018, 3, Downloaded from https://agupubs.onlinelibrary.wiley.com/doi/10.1002/2017RS006263 by Cochrane Germany, Wiley Online Library on [20/12/2022]. See the Terms and Conditions (https://onlinelibrary.wiley.com/terms-and-conditions) on Wiley Online Library for rules of use; OA articles are governed by the applicable Creative Commons License

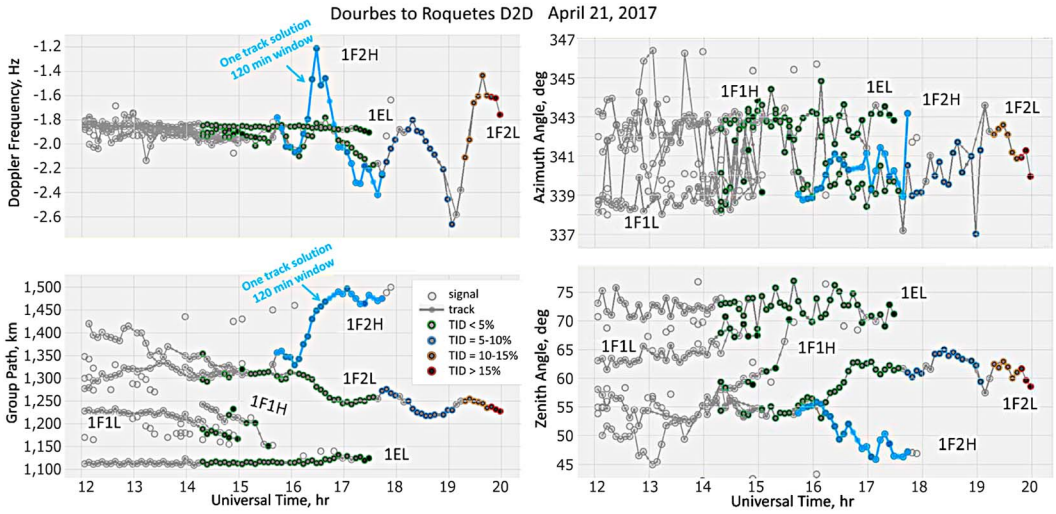

Figure 7. Automatically tracked signal parameter for the 1,083 km DB → EB link: Doppler frequency, group path length, and azimuth and zenith angles. DB = Dourbes; EB = Ebro; D2D = Digisonde-to-Digisonde.

complimentary information on the reference time, the location of the TIDs (midpoint of the D2D links, the observation metadata like the coordinates of the link endpoints, operating frequency, etc.), and the extracted time series of the RF signal characteristics $\{\rho, \delta, \varepsilon, \beta\}$. The derived TID characteristics A_N, T_Ω, V_p, and Θ for the dominant (maximum amplitude) TID wave component are also deposited in TIDBase. For TID alert applications real-time Net-TIDE FAS results are displayed every 5 min in graphical form at http://tid.space.noa.gr.

4. Assessment of the Results

The qualitative assessment of these preliminary results is primarily based on the examination of the phenomenological characteristics recorded at auroral magnetometers and on the electron isodensity contours derived from the respective vertical ionogram measurements that were made every 5 min at the Net-TIDE DPS4D observatories. The isodensity contours at the north link terminals, Pruhonice and Juliusruh, and the south link terminals, Dourbes and Ebro, are presented in Figure 9 together with the contours from the Athens DPS4D, which is the most southeastern station of the network. The density contours for the two southern observatories, Ebro and Athens, show coherent quasi-sinusoidal variations at 19–22 UT with periods around 75–110 min (Figure 9). The D2D TID measurements between Dourbes and Ebro (Figure 8) show predominantly southward propagation at 17–21 UT with azimuth angles mostly between 140° and 180°. We note that the D2D FAS technique probes the ionosphere at the midpoint of the Dourbes-Ebro link, not at the station locations. The derived TID periods (not shown in Figure 8) vary from 95 to 110 min in fair agreement with the ionogram-derived results and wavelengths around 1,370 km; the calculated TID velocities vary between 280 and 400 m/s.

On the second half of the day on 21 April 2017 continuous substorm activity of moderate intensity is recorded according to the auroral electrojet indices (not shown here). The *AE* indices correspond to the superimposed deviation of the horizontal component of the geomagnetic field from the baseline value, recorded simultaneously at all auroral geomagnetic observatories. To examine the longitudinal sequence of the auroral electrojets intensification, it is necessary to inspect magnetograms from isolated magnetometers located at the auroral oval. For this event under study, data from the Canadian Magnetic Observatory System and the International Monitor for Auroral Geomagnetic Effects network chains have been processed. The auroral magnetograms, in the form of deviation of the horizontal component (*H*) from its baseline value, recorded by four indicative stations from the Canadian Magnetic Observatory System and the International Monitor for Auroral Geomagnetic Effects chains are shown in Figure 9, top; Table 2 lists the geographic coordinates of the magnetometers used in the present analysis.

YKC (Canada) is the most westward auroral magnetometer of this chain, which recorded an intensification of the westward auroral electrojet from 14 UT to 16 UT, with a negative bay that does not exceed 500 nT. Further

1944799x, 2018, 3, Downloaded from https://agupubs.onlinelibrary.wiley.com/doi/10.1002/2017RS006263 by Cochrane Germany, Wiley Online Library on [20/12/2022]. See the Terms and Conditions (https://onlinelibrary.wiley.com/terms-and-conditions) on Wiley Online Library for rules of use; OA articles are governed by the applicable Creative Commons License

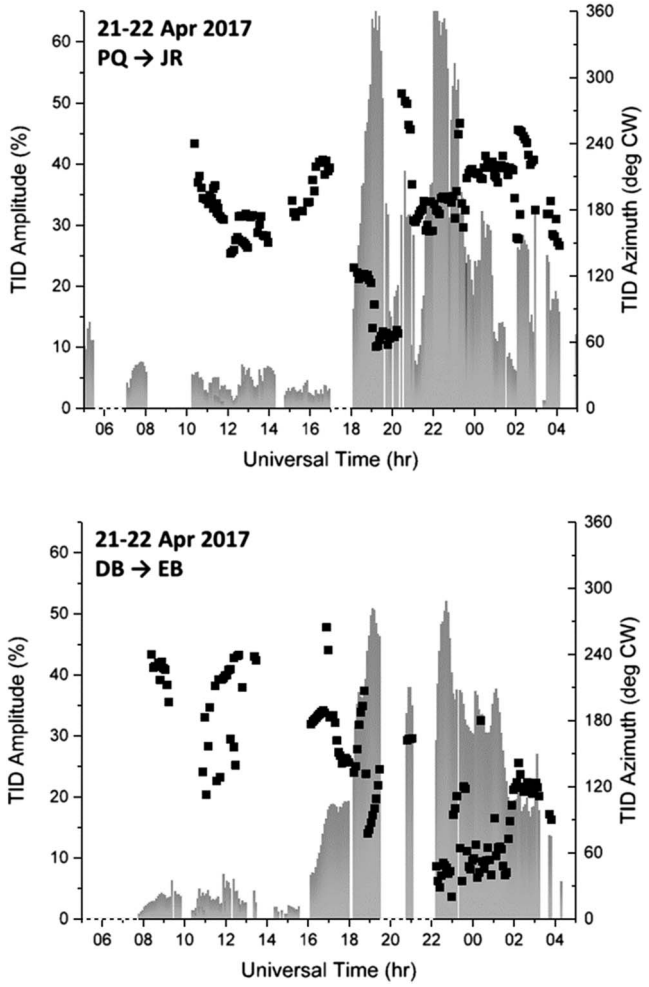

Figure 8. Doppler Frequency Angular Sounding results for TID amplitudes and propagation directions for 21–22 April 2017 derived from the (top) PQ → JR and (bottom) DB → EB link measurements. DB = Dourbes; EB = Ebro; JR = Juliusruh; PQ = Pruhonice; TID = traveling ionospheric disturbance.

to the east, IQA (Canada) observed a weaker negative bay that becomes positive at 18 UT, denoting the influence from the eastward electrojet. In RVK (Norway) weak auroral intensifications due to the eastward electrojet were observed from 17 UT to 20 UT. A stronger activity due to a westward electrojet was recorded from 21 UT until the end of the day. NUR (Finland), which is the most eastern magnetometer of the chain, is weakly affected implying that the auroral activity has a longitudinal extension that is quite limited. Nevertheless, the auroral electrojets extend thousands of kilometers along the direction of flow observed from Canadian to Scandinavian longitudes. Overall, the inspection of the magnetograms presented in Figure 9 reveals a progressive shift of the expansion of the auroral electrojets from YKC (the most westward station of the chain) to NUR (the most eastward station of the chain), while its intensity declines as it moves eastward.

Under such conditions, the atmospheric response to the auroral zone source mechanism should consist of a discrete spectrum of guided modes and a continuous spectrum of freely propagating internal waves in the upper atmosphere. This behavior suggests a pulse-like and progressive injection of energy in the auroral region ranging from the Canadian to the Scandinavian longitudes at least, which, according to Prölss's phenomenological model (Prölss, 1993), launches a wide spectrum of AGWs. These superimpose to form an impulse like traveling atmospheric disturbance that propagates with high velocity from auroral to lower latitudes, generating both LSTIDs (guided mode) and MSTIDs (freely propagating mode). The average fluctuations of the auroral electrojet are sufficient to generate freely propagating AGWs that should be detectable at large distances as TIDs. This has been proposed as a theoretical development by Francis (1975). Independent studies by Chimonas and Hines (1970), Testud et al. (1975), and Francis (1974) proved that AGW pressure pulses having as source a moderate fluctuation of the auroral electrojet are received thousands of kilometers equatorward from the source.

For the event that is analyzed here it appears that the variations seen at Ebro and Athens have their source in the auroral activity recorded earlier, between 14 UT and 17 UT, by the Canadian auroral magnetometer network. Actually, from 17:00 UT to 19:30 UT, the analysis of the D2D skymaps from the southern link (Dourbes to Ebro) gives a TID propagation with an azimuth of 180°–150° ClockWise (see Figure 8), which is consistent with the southeast propagation scenario. The D2D results for the northern link indicate propagation of TIDs from ~21 UT to the end of the day, with an azimuth of ~180°. This is consistent with the scenario of a southern directed propagation triggered by the auroral activity intensification that is recorded at the Scandinavian magnetometers, which are in almost the same meridional sector as the Digisonde observatories.

All the above suggest a plausible interpretation that the moderate auroral activity observed in the Canadian and Scandinavian auroral longitudes is the triggering source of the TIDs detected by the Digisondes in Europe. However, due to the wide region that it is under study and the limited number of observational points in the auroral and middle latitudes that keeps vast areas without monitoring coverage (e.g., the oceans), it is not possible to infer a one-to-one correspondence between the auroral intensification and the TID amplitude increase observed at the middle latitudes.

For a fair assessment of the results one should also take into account that the amplitudes of TIDs at each location are strongly related to the propagation mode, which in turn is dependent on the ambient ionospheric electron density (Hunsucker, 1982). Inspecting the isodensity contour plots shown in Figure 9, it is evident that from 17 UT onward, when the TID activity is observed in the D2D data (Figure 8), the electron density

1944799x, 2018, 3, Downloaded from https://agupubs.onlinelibrary.wiley.com/doi/10.1002/2017RS006263 by Cochrane Germany, Wiley Online Library on [20/12/2022]. See the Terms and Conditions (https://onlinelibrary.wiley.com/terms-and-conditions) on Wiley Online Library for rules of use; OA articles are governed by the applicable Creative Commons License

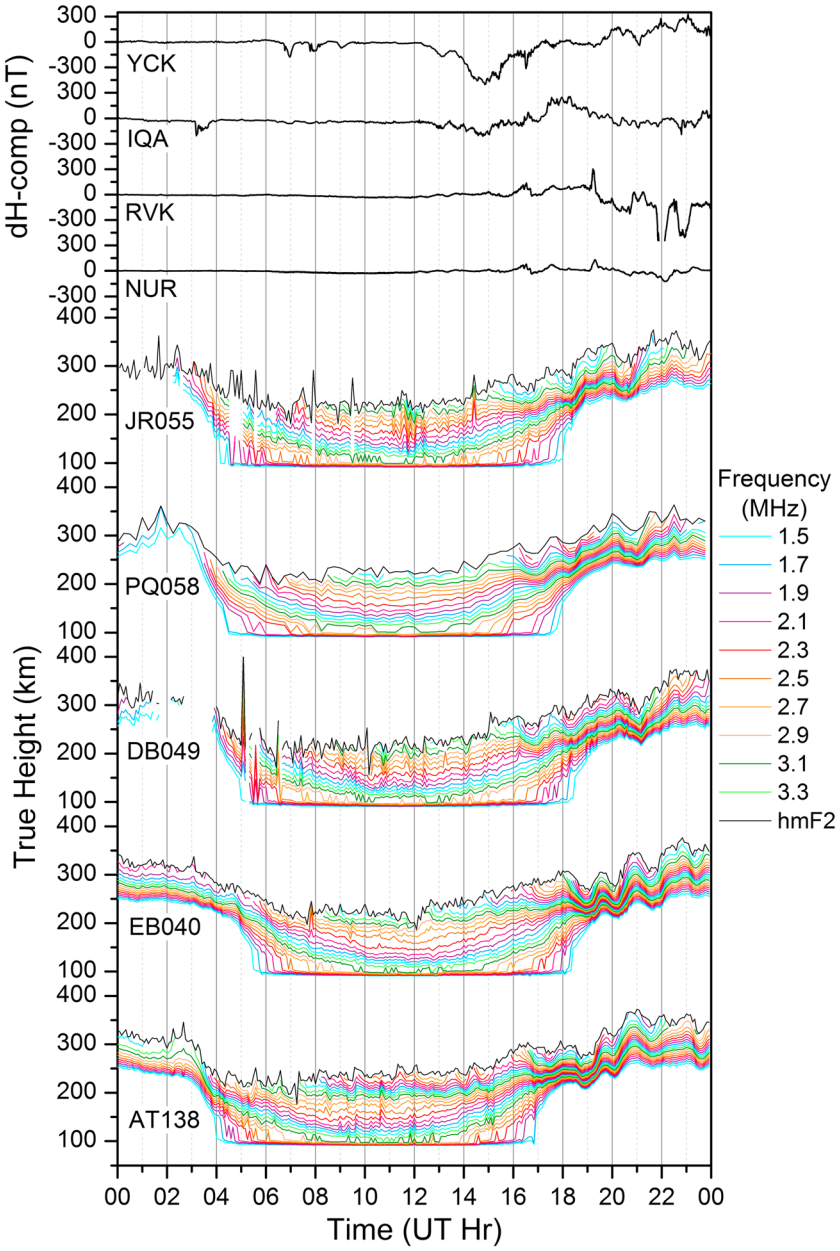

Figure 9. Isodensity contours for 21 April 2017 at Pruhonice and Juliusruh (north link), Dourbes and Ebro (south link), and Athens (the southeastern station of the Network for TID Exploration network). The variance of the *H* component from its baseline recorded at Yellowknife, Iqaluit, Rørvik, and Nurmijärvi auroral geomagnetic observatories is shown in the top.

Table 2
List of Ground-Based Magnetometers Used in the Present Analysis

Observatory	Code	Latitude (°N)	Longitude (°E)
Yellowknife	YKC	62.5	245.5
Iqaluit	IQA	63.6	291.5
Rørvik	RVK	64.9	11.0
Nurmijärvi	NUR	60.5	24.7

fluctuations with height and time have not a constant periodicity in the three higher-latitude stations, Dourbes, Juliusruh, and Pruhonice. In contrast, the electron density in Ebro and Athens exhibits a rather constant periodicity of ~2 h, indicating LSTIDs. To examine the ionospheric background conditions, the residuals of TEC from their median values over the past 15 days are shown as maps of longitude-latitude for the European region in Figure 10. These real-time maps are produced for the European region by the GNSS group of the Royal Observatory of Belgium (Bergeot et al., 2014). For the purposes of this analysis the maps have been redrawn to adjust the color code to the scales of the small TEC perturbation under study. The locations of the five

1944799x, 2018, 3, Downloaded from https://agupubs.onlinelibrary.wiley.com/doi/10.1002/2017RS006263 by Cochrane Germany, Wiley Online Library on [20/12/2022]. See the Terms and Conditions (https://onlinelibrary.wiley.com/terms-and-conditions) on Wiley Online Library for rules of use; OA articles are governed by the applicable Creative Commons License

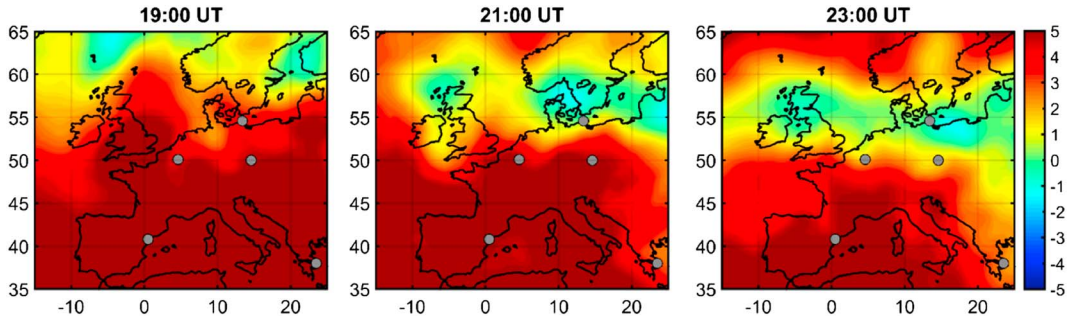

Figure 10. Maps of the residuals of the vertical total electron content from their median values for 21 April 2017 from 19 UT to 23 UT. The maps cover the area from 35°N to 63°N in latitude and from −15°E to 25°E in longitude. The gray dots indicate the positions of the Network for TID Exploration DPS4D Digisondes. The color code to the right ranges from −5 TECU to +5 TECU (Courtesy: Nicolas Bergeot, Royal Observatory of Belgium, GNSS Group).

Digisondes are marked by dots. An immediate first remark is that the electron density in the middle-latitude ionosphere is ~5 TECU higher than the median values from 19 UT to 23 UT, but at the same time this zone of high density is progressively receding equatorward. Another important remark is that at 21 UT a second zone of increased electron density appears at the higher latitudes, which extends equatorward 2 h later. In these highly variable ambient conditions, Ebro is the only station that remains in a rather steady electron density environment during the period from 19 UT to 23 UT, while Athens exhibits small variations in the ambient electron density especially after 21 UT. At the three higher-latitude stations, Juliusruh, Dourbes, and Pruhonice, the ambient electron density conditions are highly variable showing drastic increases and decreases (with respect to the median conditions) in TEC. This variable electron density environment may have resulted in different propagation modes of the AGWs and lead to variable periodicities in TIDs that may result in the isodensity contour plots of variable periodicity in Juliusruh, Dourbes, and Pruhonice.

5. Summary and Conclusions

This paper presents a new technique, based on the analysis of oblique D2D skymap observations, to directly identify TIDs and specify the TID wave parameters based on the measurement of angle of arrival, Doppler frequency, and time of flight of ionospherically reflected HF radio pulses. The novelty of the technique consists on its ability to collect, analyze, and evaluate in real-time raw observations streaming from a network of DP4D Digisondes, characterizing therefore the TID activity over a region. The paper presents the first results obtained in the framework of the Net-TIDE project of synchronizing a network of ionosondes for the automatic real-time identification of TIDs in Europe. By implementing the capability of bistatic synchronized D2D skymap measurements in DPS4D ionosondes in Europe, we are approaching the target for the automatic detection of TIDs and the determination of the direction of propagation; see http://tid.space.noa.gr.

The qualitative assessment of the results focuses on TID activities detected on 21–22 April 2017 as the result of moderate auroral activity. The inspection of auroral magnetograms in Canada and Scandinavia and of true height isodensity contours derived from the vertical incidence ionograms recorded every 5 min at the network ionosonde stations indicates the propagation of two major disturbances. The first was triggered by the auroral electrojet intensification at Canadian longitudes, directed southeastward, and affecting Europe 4 h later. The second was due to the energy released by the westward electrojet intensification in the auroral region over Scandinavia, directed almost southward and affecting European middle to high latitudes almost immediately. These observations are compatible with the TID characteristics obtained from the D2D analysis (Figure 8) and with the prevailing electron density conditions determined from the maps of TEC residuals (Figure 10). We note that a one-to-one correspondence between the auroral intensification and the wave crests in the isodensity contours is not possible because of the dispersion of the propagating ionospheric disturbances and the sparseness of the ionospheric observatories. It is also important to underline that the oscillations observed in the isodensity contours and the periodicities extracted from the D2D raw data cannot be directly and quantitatively compared because the two sets of observations do not correspond to exactly the same times and locations: the oblique D2D measurements probe the midpoint between the transmitting and receiving Digisonde, whereas the isodensity contours describe the ionosphere above each station. Because

19447998, 2018, 3, Downloaded from https://agupubs.onlinelibrary.wiley.com/doi/10.1002/2017RS006263 by Cochrane Germany, Wiley Online Library on [20/12/2022]. See the Terms and Conditions (https://onlinelibrary.wiley.com/terms-and-conditions) on Wiley Online Library for rules of use; OA articles are governed by the applicable Creative Commons License

of these restrictions the assessment of the Net-TIDE system performance can only be considered a possible interpretation and not a validation of the Net-TIDE technique.

Optimization of the Net-TIDE system performance is a key objective for the operation of a reliable TID alert system. There are currently limitations regarding the operation of the D2D links during daytime hours when nondeviative absorption in the *D* region is high, especially for the long link where the rays travel long distances in the *D* region. Quality angle-of-arrival measurements require a minimum SNR of ~40 dB, which is currently not always maintained during daytime operation. To overcome this limitation, a hardware/software modification is now being implemented in the network Digisondes that will provide a 10 dB SNR enhancement for the oblique transmissions by increasing the pulse duty cycle from 5% to 50%.

Systematic retrospective analysis of the TID data, which are progressively accumulating in TIDBase, will provide a more comprehensive overview regarding the capabilities of the D2D skymap method for the detection and specification of TIDs. This analysis will be done in the framework of the new TechTIDE project "Warning and Mitigation Technologies for TID effects," a European Commission Horizon 2020 Programme that will run until 2020 (http://tech-tide.eu). Retrospective analysis of the TID characteristics obtained from (1) GNSS TEC-based methods (Borries et al., 2016; Hernandez-Pajares et al., 2006), (2) the Net-TIDE method, and (3) 3-D electron density reconstruction models (Belehaki et al., 2016) will provide the basis for cross validating the results, considering also the prevailing conditions in the ionosphere due to geospace and lower atmosphere disturbances. Discussion of the validation results is the objective of a follow-up paper.

List of Acronyms

1EH	1-hop *E* layer high-angle ray
1EL	1-hop *E* layer low-angle ray
1F2H	1-hop F_2 layer high-angle ray
1F2L	1-hop F_2 layer low-angle ray
AGW	Atmospheric gravity wave
D2D	Digisonde-to-Digisonde
DB	Dourbes
EB	Ebro
FAS	Doppler Frequency Angular Sounding
GIRO	Global Ionosphere Radio Observatory
GNSS	Global Navigation Satellite System
HF	High Frequency
JR	Juliusruh
LSTID	Large-scale TID
MSTID	Median-scale TID
Net-TIDE	Network for TID Exploration
PQ	Pruhonice
RF	Radio frequency
SNR	Signal-to-noise ratio
TAD	Traveling atmospheric disturbance
TID	Traveling ionospheric disturbance

Acknowledgments
This work is supported by the NATO *Science for Peace and Security* project 984894 and partly by the European Commission Horizon 2020 Project 776011 TechTIDE "Warning and Mitigation Technologies of Travelling Ionospheric Disturbances Effects". B. R., I. G., and V. P. were in part supported by AFRL's SBIR project FA9453-14-C-0305 and by a subcontract from SwRI under project FA8650-16-C-9104. D. A. and E. B. have been supported by Universitat Ramon Llull grants 2016-URL-Trac-001 from Obra Social la Caixa and 2016-URL-IR-001 from Generalitat De Catalunya. D. B. and D. K. have been supported by grant P209/12/2440 from the Czech Sciences Foundation. S. S. and T. V. have been supported by the Royal Meteorological Institute via the Belgian Solar-Terrestrial Centre of Excellence (STCE). We acknowledge using data of the Global Ionosphere Radio Observatory (GIRO), http://giro.uml.edu/. The D2D skymap and ionogram data used for this research can be obtained from the corresponding GIRO databases. Magnetometer data are courtesy of the CANadian Magnetic Observatory System (CANMOS), http://geomag.nrcan.gc.ca/obs/canmos-en.php%20 and the International Monitor for Auroral Geomagnetic Effects (IMAGE) network, http://www.ava.fmi.fi/image/. The maps of TEC are downloaded from the website of the GNSS group of the Royal Observatory of Belgium (http://gnss.be/).

References

Belehaki, A., Kutiev, I., Marinov, P., Tsagouri, I., Koutroumbas, K., & Elias, P. (2016). Ionospheric electron density perturbations during the 7–10 March 2012 geomagnetic storm period. *Advances in Space Research*, *59*(4), 1041–1056. https://doi.org/10.1016/j.asr.2016.11.031

Belehaki A., Reinisch, B., Galkin, I., Altadill, D., Buresova, D., Francis, M., et al. (2015). Pilot network for identification of travelling ionospheric disturbances, Proc. 14th Int. Ionospheric Effects Symposium (IES-2015), Alexandria, Virginia, 12–14 May 2015.

Beley, V. S., Galushko, V. G., & Yampolski, Y. M. (1995). Traveling ionospheric disturbance diagnostics using HF signal trajectory parameter variations. *Radio Science*, *30*, 1739–1752. https://doi.org/10.1029/95RS01992

Bergeot, N., Chevalier, J. M., Bruyninx, C., Pottiaux, E., Aerts, W., Baire, Q., et al. (2014). Near real-time ionospheric monitoring over Europe at the Royal Observatory of Belgium using GNSS data. *Journal of Space Weather and Space Climate*, *4*, A31. https://doi.org/10.1051/swsc/2014028

Bilitza, D., Altadill, D., Zhang, Y., Mertens, C., Truhlik, V., Richards, P., et al. (2014). The International Reference Ionosphere 2012—A model of international collaboration. *Journal of Space Weather and Space Climate*, *4*, A07. https://doi.org/10.1051/swsc/2014004

19447973, 2018, 3, Downloaded from https://agupubs.onlinelibrary.wiley.com/doi/10.1002/2017RS006263 by Cochrane Germany, Wiley Online Library on [20/12/2022]. See the Terms and Conditions (https://onlinelibrary.wiley.com/terms-and-conditions) on Wiley Online Library for rules of use; OA articles are governed by the applicable Creative Commons License

Borries, C., Jakowski, N., & Wilken, V. (2009). Storm induced large scale TIDs observed in GPS derived TEC. *Annales Geophysicae*, *27*(4), 1605–1612. https://doi.org/10.5194/angeo-27-1605-2009

Borries, C., Mahrous, A. M., Ellahouny, N. M., & Badeke, R. (2016). Multiple ionospheric perturbations during the Saint Patrick's Day storm 2015 in the European-African sector. *Journal of Geophysical Research: Space Physics*, *121*, 11,333–11,345. https://doi.org/10.1002/2016JA023178

Chaggara, R., Duparc, B., Soubielle, J., Nouvel, O., & Billot, A. (2015). Characterisation of impact of scintillations over EGNOS, ION 2015. Tampa.

Chilcote, M., LaBelle, J., Lind, F. D., Coster, A. J., Miller, E. S., Galkin, I. A., & Weatherwax, A. T. (2015). Detection of traveling ionospheric disturbances by medium-frequency Doppler sounding using AM radio transmissions. *Radio Science*, *50*, 249–263. https://doi.org/10.1002/2014RS005617

Chimonas, G., & Hines, C. O. (1970). Atmospheric gravity waves launched by auroral current. *Planetary and Space Science*, *18*(4), 565–582. https://doi.org/10.1016/0032-0633(70)90132-7

Crane, L. (2017). When lower-atmosphere waves invade the upper atmosphere. *Eos*, *98*. https://doi.org/10.1029/2017EO068195

Davies, K. (1990). Ionospheric Radio. *IEE Electromagnetic Waves Series 31*. London, UK: Peter Peregrinus Ltd.

Ding, F., Wan, W., Ning, B., & Wang, M. (2007). Large-scale traveling ionospheric disturbances observed by GPS total electron content during the magnetic storm of 29–30 October 2003. *Journal of Geophysical Research*, *112*, A06309. https://doi.org/10.1029/2006JA012013

Ding, F., Wan, W., Ning, B., Zhao, B., Lin, Q., Wang, Y., et al. (2013). Observations of poleward-propagating large-scale traveling ionospheric disturbances in southern China. *Annales Geophysicae*, *31*(2), 377–385. https://doi.org/10.5194/angeo-31-377-2013

DPS4D Technical Manual (2014). [Retrieved from http://www.digisonde.com/dps-4dmanual.html.]

Federenko, Y. P., Tyrnov, O. F., Federenko, V. N., & Dorohov, V. L. (2014). Model of traveling ionospheric disturbances. *Journal of Space Weather and Space Climate*, *3*, A30. https://doi.org/10.1051/swsc/2013052

Francis, S. H. (1974). A theory of medium-scale traveling ionosphere disturbances. *Journal of Geophysical Research*, *79*, 5245–5260. https://doi.org/10.1029/JA079i034p05245

Francis, S. H. (1975). Global propagation of atmospheric gravity waves: A review. *Journal of Atmospheric and Terrestrial Physics*, *37*(6-7), 1011–1054. https://doi.org/10.1016/0021-9169(75)90012-4

Galkin, I. A., Khmyrov, G. M., Kozlov, A. V., Reinisch, B. W., Huang, X., & Paznukhov, V. V. (2008). The ARTIST 5. In *Radio sounding and plasma physics Conference*, 27 April – 3 May 2007 (Vol. 974, pp. 150–159). Lowell, MA: AIP Conference Proceedings. https://doi.org/10.1063/1.2885024

Galkin, I. A., Reinisch, B. W., Huang, X., & Bilitza, D. (2012). Assimilation of GIRO data into a real-time IRI. *Radio Science*, *47*, RS0L07. https://doi.org/10.1029/2011RS004952

Galkin, I. A., Reinisch, B. W., Ososkov, G. A., Zaznobina, E. G., & Neshyba, S. P. (1996). Feedback neural networks for ARTIST ionogram processing. *Radio Science*, *31*, 1119–1128. https://doi.org/10.1029/96RS01513

Galushko, V. G., Beley, V. S., Koloskov, A. V., Yampolski, Y. M., Paznukhov, V. V., Reinisch, B. W., et al. (2003). Frequency-and-angular HF sounding and ISR diagnostics of TIDs. *Radio Science*, *38*(6), 1102. https://doi.org/10.1029/2002RS002861

Hernandez-Pajares, M., Juan, J. M., & Sanz, J. (2006). Medium-scale traveling ionospheric disturbances affecting GPS measurements: Spatial and temporal analysis. *Journal of Geophysical Research*, *111*, A07S11. https://doi.org/10.1029/2005JA011474

Hines, C. O. (1974). *The upper atmosphere in motion*, *Geophysical Monograph*, (Vol. 18). Washington, DC: American Geophysical Union. https://doi.org/10.1029/GM018

Hocke, K., & Schlegel, K. (1996). A review of atmospheric gravity waves and travelling ionospheric disturbances: 1982–1995. *Annales Geophysicae*, *14*(9), 917–940. https://doi.org/10.1007/s00585-996-0917-6

Huang, X., & Reinisch, B. W. (2006). Real time HF raytracing through a tilted ionosphere. *Radio Science*, *41*, RS5S47. https://doi.org/10.1029/2005RS003378

Huang, X., Reinisch, B. W., Sales, G. S., Paznukhov, V. V., & Galkin, I. A. (2016). Comparing TID simulations using 3-D ray tracing and mirror reflection. *Radio Science*, *51*, 337–343. https://doi.org/10.1002/2015RS005872

Hunsucker, R. D. (1982). Atmospheric gravity waves generated in the high-latitude ionosphere: A review. *Reviews of Geophysics and Space Physics*, *20*(2), 293–315. https://doi.org/10.1029/RG020i002p00293

Liu, H.-L. (2016). Variability and predictability of the space environment as related to lower atmosphere forcing. *Space Weather*, *14*, 634–658. https://doi.org/10.1002/2016SW001450

MacDougall, J., Abdu, M. A., Batista, I., Fagundes, P. R., Sahai, Y., & Jayachandran, P. T. (2009). On the production of traveling ionospheric disturbances by atmospheric gravity waves. *Journal of Atmospheric and Solar-Terrestrial Physics*, *71*(17-18), 2013–2016. https://doi.org/10.1016/j.jastp.2009.09.006

McNamara, L. F. (1991). *The ionosphere: Communications, surveillance, and direction finding*. Malabar, Florida: Krieger Publishing Company.

Morgan, M. G., Calderón, C. H. J., & Ballard, K. A. (1978). Techniques for the study of TID's with multi-station rapid-run ionosondes. *Radio Science*, *13*, 729–741. https://doi.org/10.1029/RS013i004p00729

Murtagh, F., & Contreras, P. (2012). Algorithms for hierarchical clustering: An overview. *Wiley Interdisciplinary Reviews: Data Mining and Knowledge Discovery*, *2*(1), 86–97. https://doi.org/10.1002/widm.53

Nickisch, L. J., Hausman, M. A., & Fridman, S. V. (2006). Range rate–Doppler correlation for HF propagation in traveling ionospheric disturbance environments. *Radio Science*, *41*, RS5S39. https://doi.org/10.1029/2005RS003358

Paznukhov, V. V., Galushko, V. G., & Reinisch, B. W. (2012). Digisonde observations of AGWs/TIDs with Frequency and Angular Sounding Technique. *Advances in Space Research*, *49*(4), 700–710. https://doi.org/10.1016/j.asr.2011.11.012

Pintor, P., & Roldan, R. (2015). The impact of the high ionospheric activity in the EGNOS performance. *Coordinates Magazine*, *XI*(03).

Prölss, G. W. (1993). On explaining the local time variation of ionospheric storm effects. *Annales Geophysicae*, *11*, 1–9.

Prölss, G. W., & Ocko, M. (2000). Propagation of upper atmospheric storm effects towards lower latitudes. *Advances in Space Research*, *26*(1), 131–135. https://doi.org/10.1016/S0273-1177(99)01039-X

Reinisch, B. W., & Galkin, I. A. (2011). Global Ionospheric Radio Observatory (GIRO). *Earth, Planets and Space*, *63*(4), 377–381. https://doi.org/10.5047/eps.2011.03.001

Reinisch, B. W., Galkin, I. A., Khmyrov, G. M., Kozlov, A. V., Bibl, K., Lisysyan, I. A., et al. (2009). New Digisonde for research and monitoring applications. *Radio Science*, *44*, RS0A24. https://doi.org/10.1029/2008RS004115

Reinisch, B. W., & Huang, X. (1983). Automatic Calculation of electron density profiles from digital ionograms, 3, processing of bottomside ionograms. *Radio Science*, *18*, 477–492. https://doi.org/10.1029/RS018i003p00477

Reinisch, B. W., Paznukhov, V. V., Galkin, I. A., Altadill, D., & McElroy, J. (2008). Precise radar range measurements with Digisondes, *Radio Sounding and Plasma Physics* Conference, 27 April – 3 May 2007, (Vol. 974, pp. 144–149). Lowell, MA: AIP Conference Proceedings. https://doi.org/10.1063/1.2885022

19447973x, 2018, 3, Downloaded from https://agupubs.onlinelibrary.wiley.com/doi/10.1002/2017RS006263 by Cochrane Germany, Wiley Online Library on [20/12/2022]. See the Terms and Conditions (https://onlinelibrary.wiley.com/terms-and-conditions) on Wiley Online Library for rules of use; OA articles are governed by the applicable Creative Commons License

Ross, W. (1947). The estimation of the probable accuracy of high frequency radio direction-finding bearings. *Journal of the IEE*, *94*(Part III), 722–726.

Tedd, B. L., & Morgan, M. G. (1985). TID observations at spaced geographic locations. *Journal of Geophysical Research*, *90*, 12,307–12,319. https://doi.org/10.1029/JA090iA12p12307

Testud, J., Amayenc, P., & Blanc, M. (1975). Middle and low latitude effects of auroral disturbances from incoherent scatter. *Journal of Atmospheric and Terrestrial Physics*, *37*(6-7), 989–1009. https://doi.org/10.1016/0021-9169(75)90011-2

Tsugawa, T., Saito, A., & Otsuka, Y. (2004). A statistical study of large-scale traveling ionospheric disturbances using the GPS network in Japan. *Journal of Geophysical Research*, *109*, A06302. https://doi.org/10.1029/2003JA010302

Verhulst, T., Altadill, D., Mielich, J., Reinisch, B., Galkin, I., Mouzakis, A., et al. (2017). Vertical and oblique HF sounding with a network of synchronised ionosondes. *Advances in Space Research*, *60*(8), 1644–1656. https://doi.org/10.1016/j.asr.2017.06.033

Yakovets, A. F., Vodyannikov, V. V., Gordienko, G. I., & Litvinov, Y. G. (2013). Height profiles of the amplitudes of large-scale traveling ionospheric disturbances. *Geomagnetism and Aeronomy*, *53*(5), 655–662. https://doi.org/10.1134/S0016793213050174

19447973x, 2018, 3, Downloaded from https://agupubs.onlinelibrary.wiley.com/doi/10.1002/2017RS006263 by Cochrane Germany, Wiley Online Library on [20/12/2022]. See the Terms and Conditions (https://onlinelibrary.wiley.com/terms-and-conditions) on Wiley Online Library for rules of use; OA articles are governed by the applicable Creative Commons License